

The Multi-EAR

by

ir. O.F.C. den Ouden

Project duration:	July, 2020 – July, 2021
Collaborators:	Dr. J.D. Assink KNMI
	Dr. A. Barnhoorn TU Delft
	J.J. van den Berg TU Delft
	E.V. Donata Min. IenW
	Prof. dr. L.G. Evers TU Delft/KNMI
	G. van Schouwenburg Min. IenW
	Dr. ir. P.S.M. Smets TU Delft/KNMI

An electronic version of this thesis is available at <http://repository.tudelft.nl/>.

Contents

1	Introduction	1
2	Mobile platform design	3
2.1	Circuit design	3
2.2	Firmware	3
2.3	Raspberry Pi - an external data logger	4
2.4	LoRa Telecommunication	4
2.5	Sensors	4
2.5.1	Sound sensors	4
2.5.2	Meteorological sensors.	6
2.5.3	Inertial measurement units	8
3	Casings	9
3.1	Atmospheric dome	9
3.2	Casing designs	9
3.3	Antennae	10
3.4	External power supply	11
3.5	Autonomous system	11
4	Sensor calibration	13
4.1	Laboratory calibration	13
4.1.1	Barometric pressure	13
4.1.2	Temperature/Humidity	13
4.2	Field comparison	14
4.2.1	Meteorological observations	14
4.2.2	Sound observations	14
4.2.3	Movement observations	16
5	Outlook	19
A	Firmware update	21
B	UART serial data communication	25
C	Output sensor platform byte structure	27
D	XML metadata	29
E	SSH connection with RPi	31
F	Pictures	33
F.1	Sensor platform.	33
F.2	Small casing - (serial numbers 3001 - 3022)	34
F.3	Large casing - (serial numbers 3101 - 3108)	35
F.4	Power supply	36
F.5	Antenna's	36
G	Low-costs sensor platform	37

Introduction

Geophysical studies and real-time monitoring of natural hazards, such as volcanic eruptions or severe weather events, benefit from joint analysis of multiple geophysical parameters. However, current geophysical measurement platforms typically provide data acquisition for a single parameter only due to the large variety in possible configurations. Often such multi-parameter platforms need to be built on demand and are therefore relatively expensive.

Within this document, the Multi Earth and Atmospheric data Recorder (Multi-EAR) is introduced. The Multi-EAR is a mobile, low-cost multidisciplinary sensor platform for scientific monitoring of the earth and atmosphere. The platform can complement existing high-quality, commercial sensor networks. Our new platforms are designed using digital Micro-electromechanical Systems (MEMS) sensors embedded on a Printed Circuit Board (PCB). Due to the low power consumption of MEMS, the system can be powered by a battery or solar panel.

Various disciplines are applying MEMS sensor technology to obtain higher spatial and temporal resolution data (D'Alessandro et al., 2014). MEMS are small single-chip sensors, combining electrical and mechanical components, and have a low energy consumption. The seismic community has created low-cost, reliable MEMS accelerometers for various applications (Homeijer et al., 2011). The infrasound community (Anderson et al., 2018; Marcillo et al., 2012), as well as the meteorological society are integrating MEMS into the existing sensor network (Fang et al., 2010; Huang et al., 2003; Ma et al., 2011). Nonetheless, MEMS are also known to be less accurate than conventional high-fidelity equipment. Especially digital MEMS sensors, which have an in-build Analog-Digital-Converter (ADC), are known for their high self-noise level.

The Multi-EAR is an extension of the INFRA-EAR (den Ouden et al., 2021), which is a multidisciplinary sensor platform for the monitoring of geophysical parameters, and specially designed to fit a Wandering Albatross. Such requirements, and thus dimensional restrictions, were not applicable by the design and development of the Multi-EAR. This project aims to develop, based on earlier recommendations, a multidisciplinary mobile sensor platform to complement the existing high-fidelity monitoring network. Due to its digital design, the sensor platform can readily be integrated with existing geophysical data infrastructures and be embedded in geophysical data analysis. The small dimensions and low-cost price per unit allow for unconventional, experimental designs, for example, high-density spatial sampling or deployment on moving measurement platforms. Moreover, such deployments can complement existing high-fidelity geophysical sensor networks. To include the Multi-EAR within existing monitoring networks, a Technology Readiness Level (TRL) of 8 is needed (Figure 1.1).

Research grant

The Multi-EAR is a successor of the INFRA-EAR. The project has been submitted and awarded the 'Digitaliserings-fonds en Ontwikkeling' research grant by the Netherlands Ministry of Infrastructure and Water Management and an 'Innovation' grant by the Delft University of Technology.

Therefore, the Multi-EAR is a collaborative project between the Royal Netherlands Meteorological Institute (KNMI) and Delft University of Technology (TU Delft).

Outline

This document is the technical report of the Multi-EAR. The chapters will informatively describe the sensor platform. Chapter 2 discusses the sensors on the board, their response functions and the accuracy/tolerance. Chapter 3 describes the design of the casings. Two different casings are designed. The smaller casings are for rapid deployment, whereas the larger casings are entirely autonomous and serve remote places. The calibration and comparison study of the Multi-EAR is highlighted within Chapter 4. The conclusion, discussion, and next steps of the project are discussed in Chapter 5.

The appendixes provide technical descriptions of some of the topics highlighted within the Chapters. The complete description, codes, firmware, software, and STEP files of the Multi-EAR are available on the [GitHub page](#). The GitHub repository will be an up-to-date database for information regarding the Multi-EAR.

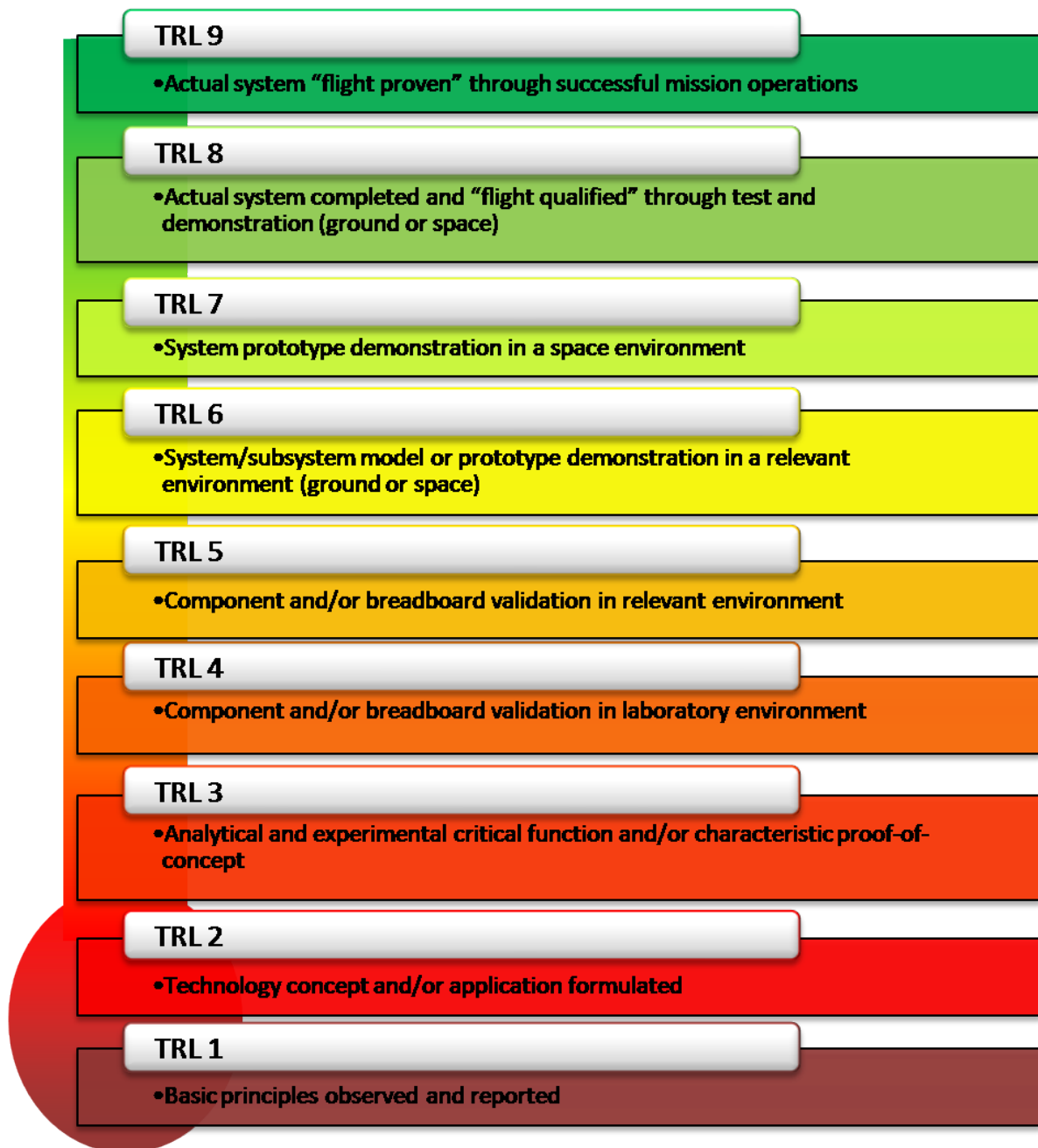


Figure 1.1: Technology Readiness Levels (TRL) are a measure to assess the maturity level of a particular technology. There are nine technology readiness levels, TRL 1 is the lowest and TRL 9 is the highest.

2

Mobile platform design

2.1. Circuit design

The platform of the Multi-EAR uses various digital Microelectromechanical sensors (MEMS) embedded on a Printed Circuit Board (PCB). A programmable microcontroller unit, embedded on the PCB, controls the sensor's sampling frequency, establishes the energy supply for the sensors, the data communication, and data storage.

The MEMS on the PCB are; two differential pressure sensors (to monitor infrasound), a 6-axis accelerometer/gyroscope, a 6-axis accelerometer/magnetometer, a barometric pressure sensor, a temperature/humidity sensor, microphones (to monitor audible sound), a GPS for location and timing purposes, and LoRa telecommunication for data exchange.

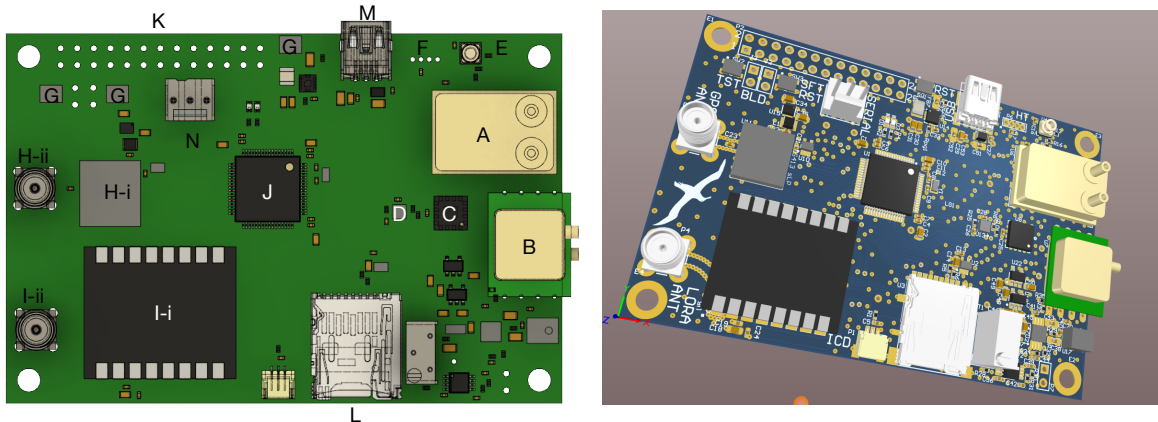


Figure 2.1: 3D CAD design of the Multi-EAR. (a) The top view of the PCB, and (b) the 3D STEP file. The PCB hosts; a Superior Sensor SP200 differential pressure sensor (A), All-Sensor DLVR-F50D differential pressure sensor (B), an ST Electronics LSM303 6-axis accelerometer/magnetometer (C), LIS3DH 6-axis accelerometer/gyroscope (D), ST Electronics LPS33HW barometric pressure sensor (E), Sensirion SHT8x temperature and humidity sensor (F), 3 ICS microphones (G), a Texim GN2301 (H) and LoRa telecommunication (I) connected to LINX passive antenna's (-i), and an MSP430 Texas instruments microcontroller (J). The platform either be powered over the GPIO pins (K) or via mini-USB (M). The data can be stored on the microcontroller's flash memory, locally on a micro-SD card (L), or an external device connected over the GPIO pins.

2.2. Firmware

The communication between the microcontroller and MEMS on the PCB is either done by Inter-Integrated Circuit (I2C) or Serial Peripheral Interface (SPI) and depends on the sensor and personal preference. Both communication methods are bus protocols and allow for serial data transfer. However, SPI handles full-duplex communication, simultaneous communication between microcontroller and MEMS sensor, while I2C is half-duplex. Therefore, I2C has the option of clock stretching, and the communication

is stopped whenever the MEMS sensor cannot send data. Besides, I2C has built-in features to verify the data communication (e.g., start/stop bit, acknowledgement of data). Although the I2C protocol is favourable, it requires more power. Moreover, the number of I2C ports on the microcontroller is limited. Therefore a mix of both SPI and I2C protocols is needed.

The microcontroller runs on self-made software, complementing the required manufacturers electrical and communication protocols. The software allows determining the sample time, sample frequency, and data storage of selected MEMS. The raw output of the digital MEMS sensors are stored as bits, and the microcontroller performs no data processing to save power consumption.

The firmware, and thus the data acquisition, can be changed and updated on the microcontroller following Appendix A.

2.3. Raspberry Pi - an external data logger

The microcontroller communicates in two ways with the MEMS. After sampling, the MEMS send their data back to the microcontroller. The data can be stored locally on the PCB, using a micro-SD card, or sent through UART serial communication. The PCB embeds GPIO pins, which allow UART communication. The GPIO allows a connection between the PCB and a Raspberry Pi (RPi, “Technical Report Raspberry Pi Model 3B+”, 2018), and thus the data communication between both. The RPi can therefore act as a small datalogger. The RPi receives on a pre-specified baud-rate the data in bytes (Appendix B).

The received data, the output of the Multi-EAR, is described within Appendix C. Per sample cycle, the bytes are sent in a pre-specified byte structure. First, the synchronization bytes are sent when after the payload with actual data follows. The format of the stored data on the RPi is either Level 0 (bytes) or Level 1 (floats) data.

The metadata of the Multi-EAR can be found within the XML files (Appendix D). Within these files, the response functions of the sensors are stored, as well as the transformation constants to convert the bytes/floats into actual geophysical units.

The RPi is an ideal data logger because it is a small single-board computer and has all the usual connections (i.e., HDMI, USB, Micro-USB). The operating system on the RPi’s of the Multi-EAR is ‘raspbian-lite’ and can connect with WiFi. The data can be accessed directly on the RPi or be transferred towards an external device. A data bridge is facilitated via WiFi or an SSH connection (Appendix E).

2.4. LoRa Telecommunication

Besides transferring data via the RPi and WiFi, the data can also be transferred by LoRa Telecommunication (“Technical Report LoRa Telecommunication”, 2021). LoRa is a type of wireless telecommunication vast area network designed to allow long-range communications at a low bit rate among things (connected objects). The low power, low bit rate and intended use distinguish this type of network from a wireless WAN designed to connect users or businesses and carry more data, using more power. The LoRa data rate ranges from 0.3 kbit/s to 50 kbit/s per channel. LoRa may be used to create a private wireless sensor network but may also be a service or infrastructure offered by a third party, allowing the owners of sensors to deploy them in the field without investing in gateway technology.

2.5. Sensors

2.5.1. Sound sensors

The human audible sound spectrum is approximately between 20 to 20,000 Hz. Frequencies below 20 Hz or above 20 kHz are referred to as infrasound and ultrasound, respectively. The movement of large air volumes generates infrasound signals with amplitudes in millipascals’ range to tens of pascals. Examples of infrasound sources include earthquakes, lightning, meteors, nuclear explosions, interfering oceanic waves and surf (Campus and Christie, 2010). Detection of infrasound depends on the signal’s strength relative to the noise levels at a remote sensor (array), i.e., the signal-to-noise ratio. The signal strength depends, in turn, on the transmission loss that a signal experiences while propagating from source to receiver (Waxler and Assink, 2019). Local wind noise conditions predominantly determine the noise (Raspel et al., 2019), in addition to the sensor self-noise. Due to the presence of atmospheric waveguides and low absorption at the infrasonic frequency (Sutherland and Bass, 2004), infrasonic signals can be detected at long distances from an infrasonic source. Assumed that the source levels

are sufficiently high so that the long-range signal is above the ambient noise conditions on the receiver side, and the sensor is sensitive enough to detect the signal.

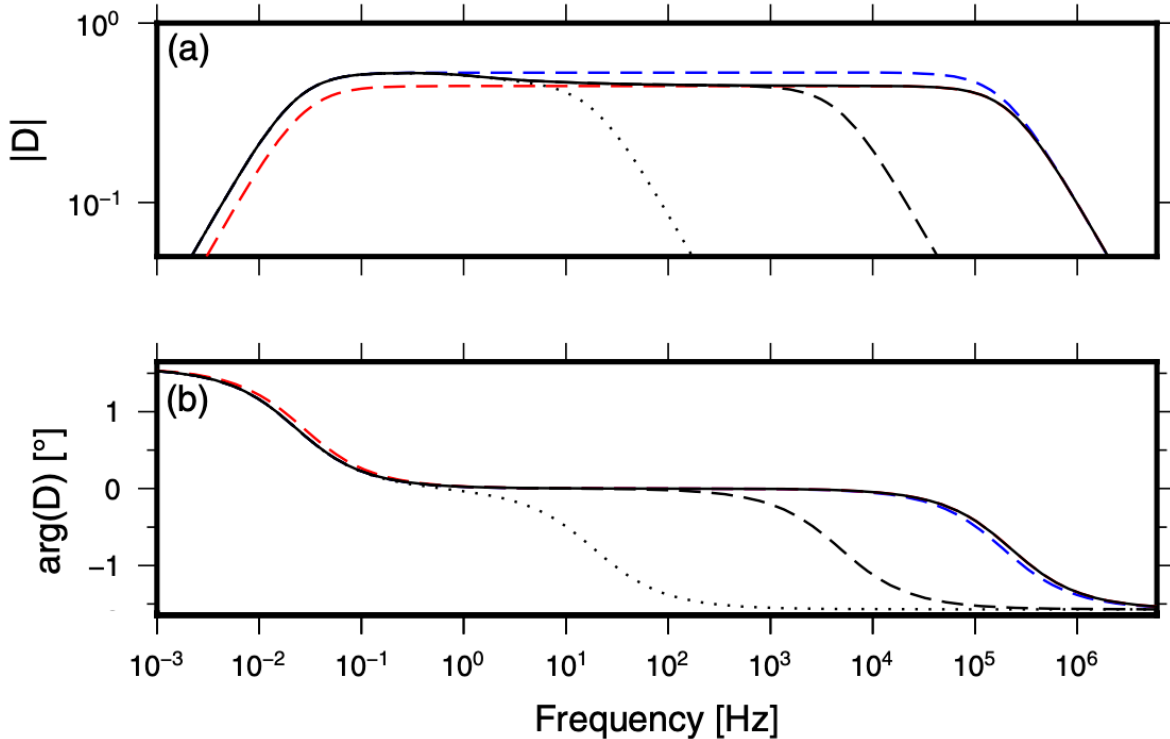


Figure 2.2: The response curves of the KNMI-mb. Panel a shows the amplitude response over the frequency range. Panel b the phase response.

Infrasound

The infrasonic wavefield is conventionally measured with pressure transducers since such scalar measurements are relatively easy to perform. Those measurements can either be performed by absolute or differential pressure sensors. An absolute pressure sensor consists of a sealed aneroid and a measuring cavity connected to the atmosphere. A pressure difference within the measuring cavity will deflect the aneroid capsule. The mechanical deflection is converted to a voltage (Haak and De Wilde, 1996). The measurement principle of a differential infrasound sensor relies on the deflection of a compliant diaphragm, which is mounted on a cavity inside the sensor. The membrane deflects due to a pressure difference inside and outside the microphone, which occurs when a sound wave passes. A pressure equalization vent is part of the design to make the microphone insensitive to slowly varying pressure differences originating from long-period changes in weather conditions (Ponceau and Bosca, 2010).

Various studies show sensor self-noise and sensitivity curves of infrasound sensors (Marty, 2019; Merchant, 2015; Nief et al., 2019; Ponceau and Bosca, 2010; Slad and Merchant, 2016). The IMS specifications state that the sensor self-noise should be at least 18 dB below the global low noise curves at 1 Hz (Brown et al., 2014), generated from global infrasound measurements using the IMS. Typical infrasound sensor networks, such as the IMS, use analogue sensors connected to a separate data logger to convert the measured voltage differences to a digital signal. The sensor's characteristic sensitivity determines the sensor resolution, i.e., the smallest difference that the sensor can detect. The resolution of the built-in analogue-to-digital converters (ADC) and the digitizing voltage range determine the datalogger's resolution. Current state-of-the-art data loggers have a 24-bit resolution. New infrasound sensor techniques involve digital outputs since the ADC conversion is realized inside the sensor (Nief et al., 2019).

The design of this instrument is based on the following requirements. The sensor should have a flat, linear response over a wide infrasonic frequency band, e.g., 0.05 - 10 Hz. The sensor should be sensitive to the range of pressure perturbations in this frequency band, ranging from millipascals to

tens of pascals. Moreover, the sensor and logging components' self-noise should be below the ambient noise levels of the IMS (Brown et al., 2014). Taking this into account, the sensor requires as well to be low-cost (i.e., tens of dollars), small in dimensions (i.e., millimetre), and have a low energy consumption (i.e., milliampere).

The measurement principle relies on the deflection of a diaphragm, which is mounted between two inlets. One inlet is connected to the atmosphere, while the other is connected to a cavity. The digital MEMS DLVR-F50D differential pressure sensor from All Sensors Inc ("Technical Report DLVR Series Low Voltage Digital Pressure Sensors", 2019) is used as a sensing element within the mini-MB. This sensor has a 16.5mm x 13.0mm x 7.3mm dimension and a linear response between ± 125 Pa and a maximum error band of ± 0.7 Pa. A Wheatstone bridge senses the diaphragm's deflection by measuring the changes in the piezo-resistive elements attached to the diaphragm. The sensor's output is an analogue voltage, which is subsequently digitized by the built-in 14-bit ADC, offering a maximum resolution of 0.02 Pa/count.

Figure 2.2 shows the theoretical sensor response of the KNMI-mb (den Ouden et al., 2021).

Audible sound

For the monitoring of the audible sound spectrum, three ICS-40300 microphones are embedded on the PCB ("Technical Report ICS-40300 microphone", 2021). These microphones are low-noise, high SPL MEMS microphones with an extended low-frequency response. The frequency response can be extended from 6 – 20k Hz and has a flat response between 50 – 2500 Hz (Figure 2.3). Thanks to the frequency range, combining the infrasound sensor and the microphones results in an excellent phase and amplitude characteristic within a broad frequency range (0.075 - 20k Hz). The maximum SPL level of the microphones is 130dB before the overload is reached.

The measurements of the microphones are by default stored as RMS dB SPL level over the entire frequency range. Whenever an RPi is used as a data logger, there is an option to store the entire time series recording.

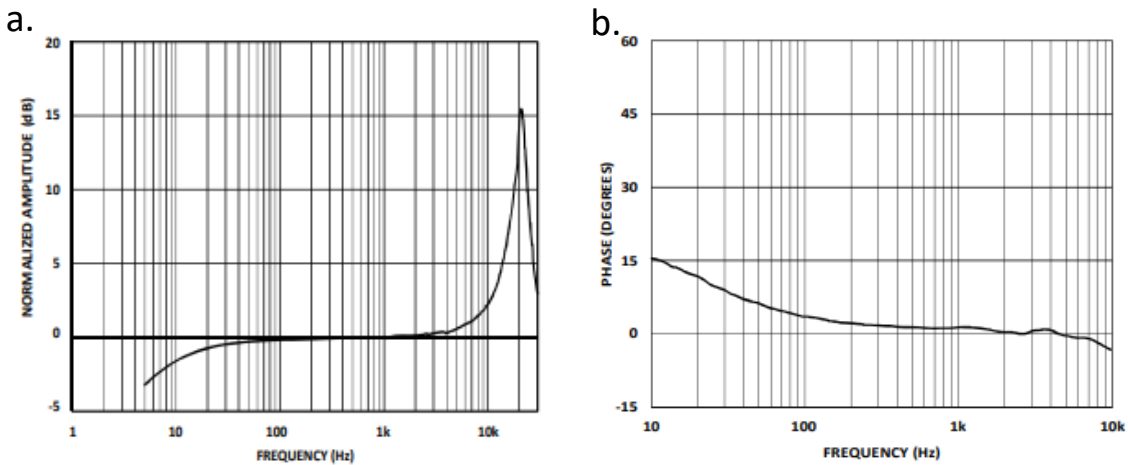


Figure 2.3: The response curves of the embedded microphones. Panel a shows the amplitude response over the frequency range. Panel b the phase response.

2.5.2. Meteorological sensors

Infrasound detectability is directly linked to local noise conditions and the atmosphere's stability in the infrasound sensor's surroundings since noise levels are increased when turbulence levels are high. Therefore, it is beneficial to have simultaneous measurements of the basic meteorological parameters,

i.e., pressure, humidity and temperature. The sub-sections below describe the different meteorological measurements contained on the sensor platform.

Barometer

The barometric pressure is sensed by the LPS33HW sensor (“Technical Report STMicroelectronics LPS33HW”, n.d.). The measuring principle relies on piezo-resistive crystals. The atmospheric pressure applies a force to the sensor, which causes the crystals to vibrate. Whenever piezo-resistive crystals have contact or a force is applied to them, a small voltage is released.

The sensor design is analogue, using voltages to derive the geophysical units. However, this MEMS has an in-built 14-bits ADC. The ADC bits and the precision of the crystals determine the self-noise of the sensor. Whenever the self-noise is higher than the actual change in atmospheric pressure, it will not be resolved by the sensor. The manufacturer states that the relative error of the sensor is $\pm 0.1\text{hPa}$. However, the absolute error can be more significant. Therefore a calibration needs to be performed on these sensors to remove the absolute error. den Ouden et al., 2021 stated that after calibration, the sensor could indeed have an accuracy of $\pm 0.1 \text{ hPa}$.

Temperature/Humidity

The SHT8x sensor measures the temperature and humidity at the PCB (“Technical Report SHT8x temperature/humidity sensor”, 2021). The SHT8x is a temperature and humidity sensor with a pin-type connector. This connector allows easy integration and replacement of the sensor. Furthermore, it allows for the best possible thermal coupling to the environment and decoupling from potential heat sources on the PCB. The sensing is done by the SHT3x sensor, which is part of the SHT8x set-up. The SHT8x has an in-built 16-bit ADC.

The humidity is sensed over the range of $0 - 100\pm$. The SHT3x has a resolution of $0.01\pm$, with a relative error of $1.5\pm$. The absolute error needs to be determined by calibration.

The operating range of the temperature sensor is between $-40 - 105^\circ\text{C}$. The resolution is 0.01°C , with a relative error of 0.3°C while operating over the entire temperature range.

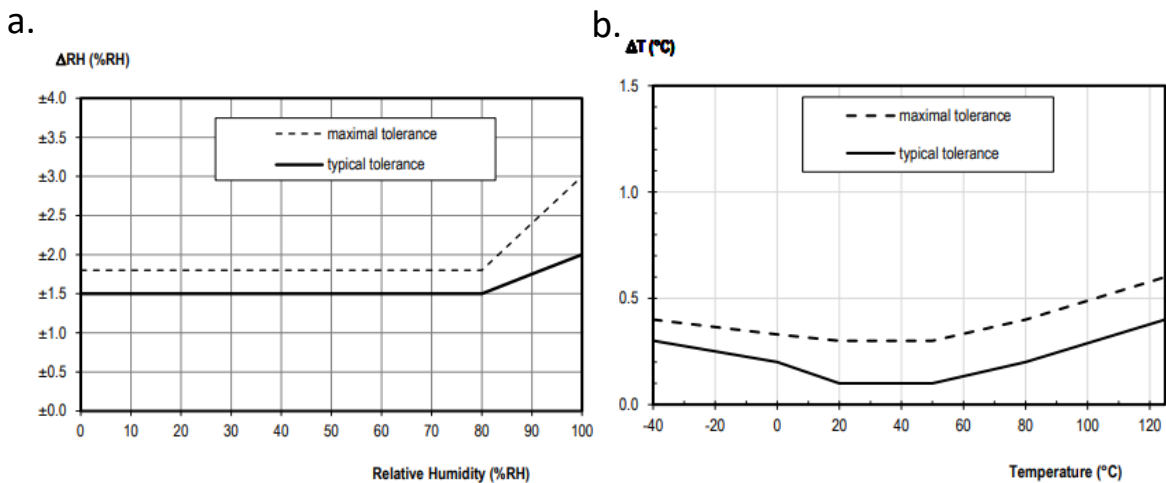


Figure 2.4: Sensitivity curves of the SHT3x MEMS sensor. Panel a shows the expected tolerance of the humidity sensor over the measurement range. Panel b shows the tolerance of the temperature sensor.

2.5.3. Inertial measurement units

The sensing element of the infrasound sensor on this platform is a sensitive diaphragm. Strong accelerations of the platform will cause a deflection of the diaphragm and may obscure infrasonic signal levels. In addition, such accelerations may be misinterpreted as infrasound if no independent accelerometer information is available. To be able to separate the mechanical response of the sensor from actual signals of interest, the platform measures accelerations for which the LSM303 (“Technical Report STMicroelectronics LSM303”, n.d.), a 6-axis inertial measurement unit, and LIS3DH (“Technical Report LIS3DH MEMS sensor”, 2021), as well a 6-axis inertial measurement unit, are deployed. The LSM303 consists of a 3-axis accelerometer and a 3-axis magnetometer. The LIS3DH is a 3-axis accelerometer and 3-axis gyroscope. The measurement range of both accelerometers varies between 2-16 g.

Accelerometers measure differential movement between the gravitational field vector and its reference frame. In the absence of linear acceleration, the sensor measures the rotated gravitational field vector, which can calibrate the sensor. A rotational movement of the sensor will result in acceleration. Both MEMS are digital sensors with built-in ADC's of 16-bit, which results in a resolution of 0.06 mg when choosing the lowest measurement range.

3

Casings

The protection of the PCB is done with a weather- and waterproof casing. The RPi and Multi-EAR PCB are connected by the GPIO pins, and for extra insurance four screws on the corners. The casing exists of a pre-ordered polyethene case with an atmospheric dome on top. The RPi is mounted to the casing, by a 3D-printed ground-plate, for direct coupling.

3.1. Atmospheric dome

An atmospheric dome is placed on top of the casing, fastened with screws and glue. The dome allows air to flow in and out of the casing, essential for the atmospheric measurements, but deducts water to enter the casing. Figure 3.1 shows the 3D CAD design of the dome. Air can flow into the dome via the inlets on the side and top of the capture. This way, the dome enables airflow inside the casing but obstructs water. Whenever moisture becomes a problem, GoreTex air vents may be considered (den Ouden et al., 2021). These air-vents should be placed on the inlet of the dome. Furthermore, the design of the dome may prevent stagnation pressure, which potentially masks differential pressure perturbations (Raspel et al., 2019). Thanks to the design, the Multi-EAR samples the surrounding air, instead of one particular flow. This way, potential stagnation pressure is balanced.

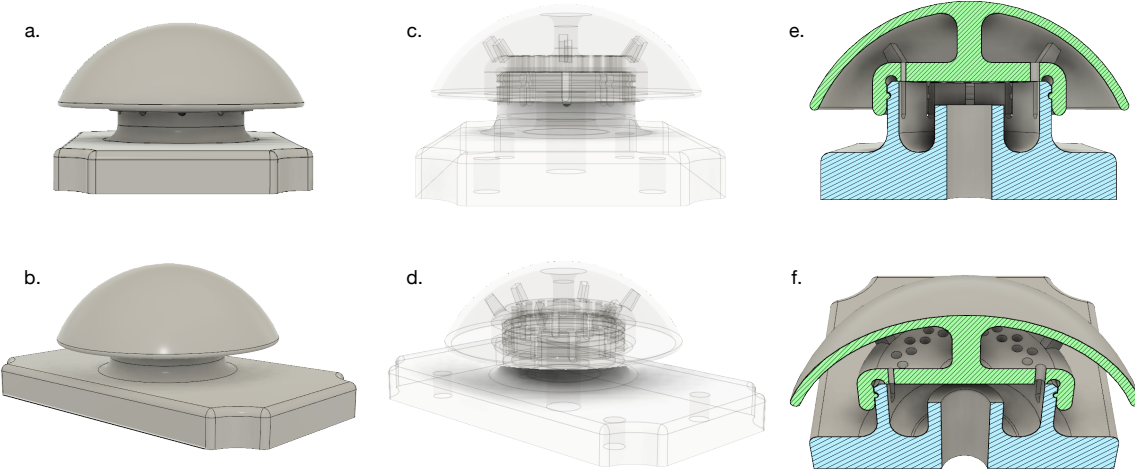


Figure 3.1: 3D CAD design of the dome. (a) and (b) show the solid outline of the dome, (c) and (d) the transparent outline, (e) and (f) the cross sections.

3.2. Casing designs

Two different casings are designed and developed for the Multi-EAR (Appendix F). The smaller casing ("Technical Report Small Casing", 2021) has a dimension of 130 x 85 x 115 mm (Figure 3.2). The dome

is placed on top of the transparent lid of the casing, while two antennas are mounted to the side, as well as the external power supply plug. The smaller casings are not autonomous, it does not function without connection to an external power supply. Whenever powered, the Multi-EAR starts recording and collecting data, as pre-defined in the firmware.

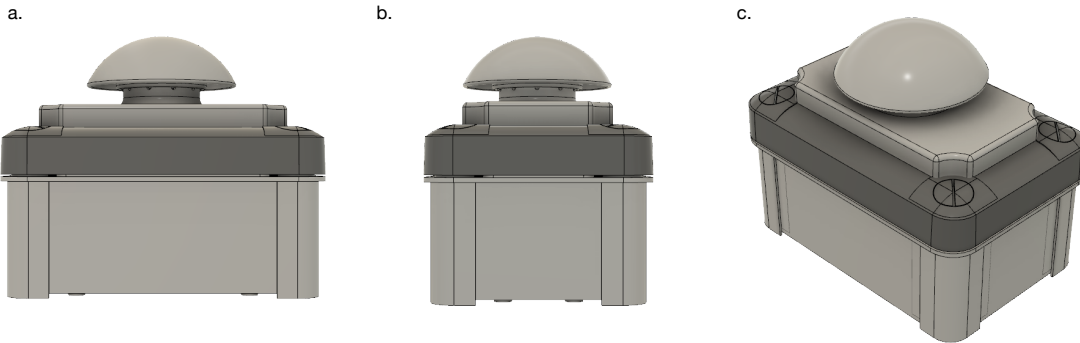


Figure 3.2: CAD-drawings of the small casing design for the Multi-EAR. The dimensions of this casing are; 130 x 85 x 115 mm.

The larger casings have a dimension of 240 x 191 x 130 mm (“Technical Report Large Casing”, 2021) and includes an external solar panel. These casings are designed to create a completely autonomous sensor platform. Again a polyethylene case with the atmospheric dome on top is used. The GPS and LoRa antenna are connected to the outside of the casing, as well as the external power plug.

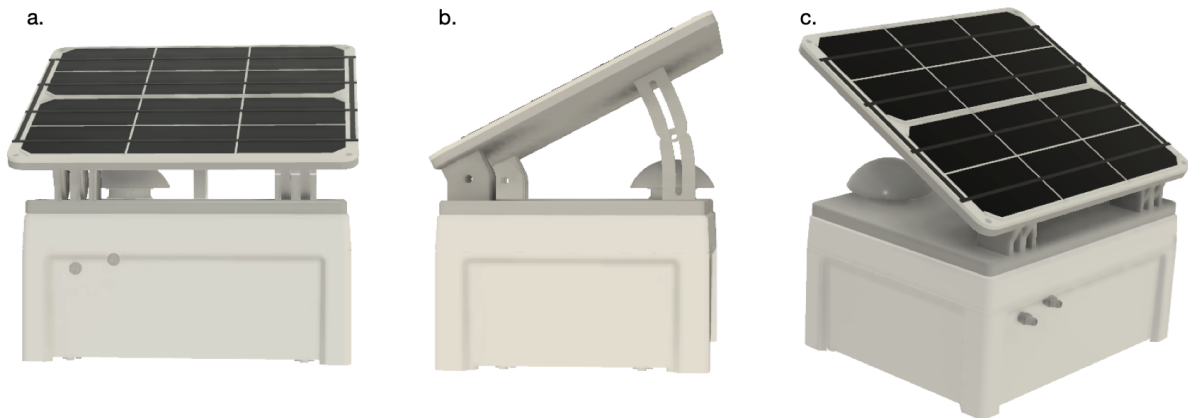


Figure 3.3: CAD-drawings of the large casing design for the Multi-EAR. The dimensions of this casing are; 240 x 191 x 130 mm.

3.3. Antennae

The LoRa and GPS on the PCB are both connected to external antenna's. The antennae are passive LinX antennae (“Technical Report Linx antenna”, 2021). The frequency range of the antenna are shifting between 617MHz - 5 GHz. For optimal signal coverage, a high-blade positioning is suggested.

The polarization of the antennae is linear, and the radiation of signals omnidirectional. Moreover, the GPS on the PCB is a GNSS receiver (“Technical Report Texim Europe GNS2301”, n.d.) and thus compatible with GPS (global system), GLONASS (Russian navigational system), Beidou (Chinese navigational system), Galileo (European navigational system). Therefore the PCB has perfect GPS coverage.

The antennae are mounted to the outside of the casings and connected to the MEMS of the GPS and LoRa by SMA extension cables (“Technical Report SMA cable”, 2021, Appendix F).

3.4. External power supply

5W micro-USB connectors generate the external power supply. The cable is modified to ensure the complete protection of the casing. Moreover, the modification allows disconnecting the power supply from the outside without creating modifications within the casing.

Within the casing, the RPi is connected through Micro-USB with a female Amphenol connector (“Technical Report Amphenol three pin connector”, 2018, Appendix F). The female connector is pinned to the outside of the casing. The male connector is directly connected to a 5W adaptor. The connection between male and female connectors is robust and weather/waterproof. Figure 3.4 shows the ‘three-pin’ layout of the Amphenol connectors.

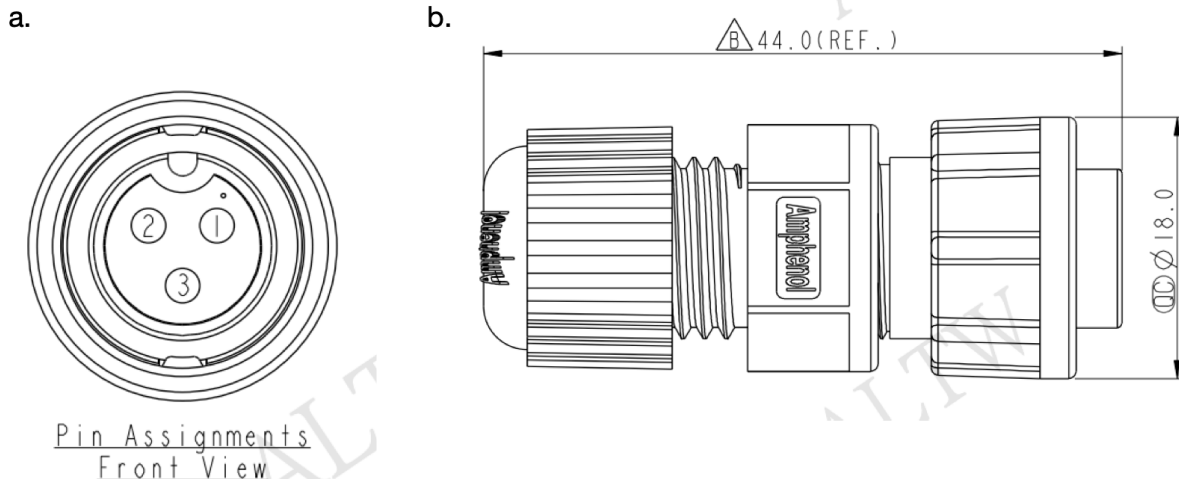


Figure 3.4: Amphenol connector. Panel a shows the front view of the pin assignments. Pin 1 is the power supply, Pin 2 the ground, while Pin 3 remains available. Panel b shows the side view of the connected male and female connector.

3.5. Autonomous system

The large casings are equipped with a solar panel (“Technical Report 9W, 6V, Solar panel”, 2020) and battery pack (“Technical Report V75 Battery Pack”, 2020). These platforms can either be powered by an external power supply or by a battery pack. The battery pack is a V75 battery and is placed within the casing. It has an ‘always-on mode; it can power, charge, and pass-through while charging. The capacity is 19.200 mAh (71 Watt-Hours), and has a 5V output.

The external solar panel charges the V75 battery pack, and is positioned at the lid of the casing. The angle of solar panel may be modified towards the sunlight’s angle. The panel is waterproof and has a 9Watt, 6V output.

Energy analysis

To determine whether the autonomous system can monitor continuously, an energy analysis is performed. The energy analysis is divided into (1) the energy consumption by the PCB and RPi during concurrently continuous monitoring and the (2) power supply by the solar panel and battery capacity to survive the evenings.

Power consumption Multi-EAR The energy consumption of the sensor platform can be divided into the consumption by the RPi and the PCB/MEMS. Assuming continuous measurements and thus power supply, the RPi will approximately use 1 Watt per hour, which adds to a maximum of 24 Watt per day.

The consumption by the PCB depends on the low-energy MEMS sensors, which is marginal compared to other monitoring devices. The power consumption is estimated at around 5W per day, which is 0.2 Watt per hour.

The total power consumption of the entire monitoring system is estimated to be approximately 29 Watt per day, 1.2 Watt per hour.

Power supply The V75 battery pack has a maximum capacity of 71 Watt. Without charging the bat-

ter pack, the monitoring system can therefore be active for approximately 70 hours. During summer, the time between sunset and sunlight is approximately 6 hours. Therefore it is assumed the system will 'survive' the summer evenings. In winter, the nights are longer, and therefore the re-charging time of the battery is shorter. The monitoring system is assumed to run out of power during the winter periods.

With day-light, the battery pack will potentially charge itself and power the monitoring system. An analysis on solar power has been performed to determine the expected charging energy of the solar panel. For the analysis, the solar panel has positioned at the Campus of the TU Delft. Based on the technical specifications of the 9 Watt solar panel, and the expected sunlight at the Campus, the energy analysis is calculated ("EU SCIENCE HUB; PVGIS", 2021).

Figure 3.5 shows the average energy output of the solar panel in Watt per day. Note that from March until September, the Solar panel provides supplies more power than needed by the Multi-EAR. During these periods, the battery will be charged during the day. Within the winter months, however, the solar panel does not provide enough power to charge the battery. Therefore, it is assumed that after a while the Multi-EAR will run out of power/battery. The battery and solar panel will not provide sufficient power for continuous and concurrent monitoring during the winter period.

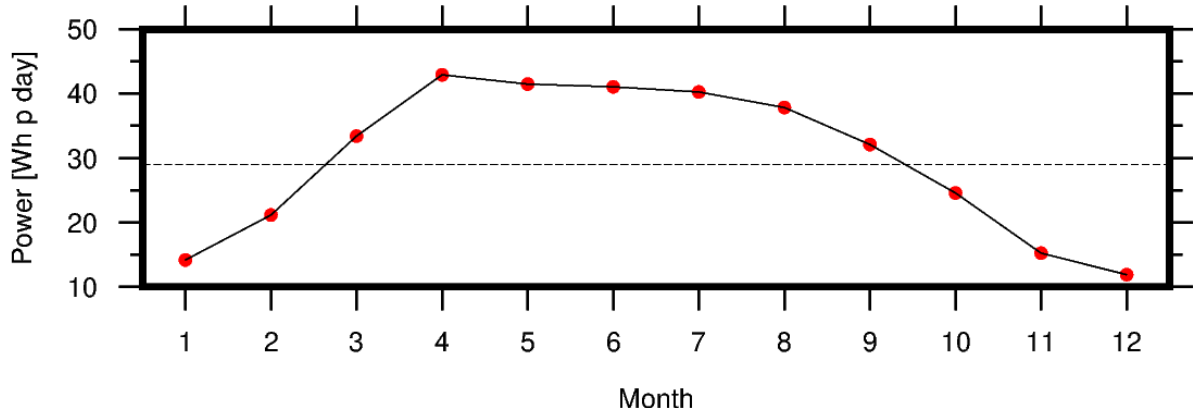


Figure 3.5: Performance of the 9Watt, 6Volt, solar panel. The red dots indicate the average daily power provided by the solar panel per day. The dotted line shows the required power per day by the monitoring system. When the provided power is larger than the required power the battery will be charged.

4

Sensor calibration

The sensor calibration and comparison have been performed according to the KNMI-calibration standards within the KNMI calibration lab. Besides lab calibrations, the sensor platform has also been placed on the KNMI test field, enabling a comparison of the platform with high-fidelity equipment.

4.1. Laboratory calibration

4.1.1. Barometric pressure

Calibration tests on the barometric pressure sensor are performed within a pressure chamber, in which a cycle of static pressures between 930 and 1070 hPa can be produced. Besides the MEMS sensor, the chamber is equipped with a reference sensor. This procedure resulted in a calibration curve, which describes the pressure-dependent systematic bias. After correcting for the bias, the LPS sensor has an accuracy of ± 0.1 hPa, i.e., the LPS sensors measures values within ± 0.1 hPa of the value measured by the KNMI reference sensor.

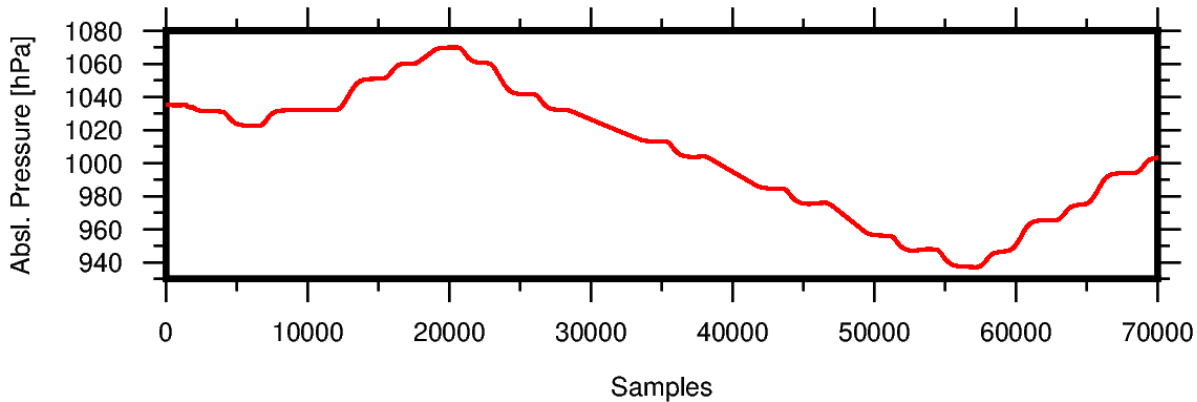


Figure 4.1: Calibration curve of the barometric pressure sensor.

4.1.2. Temperature/Humidity

The calibration tests on the temperature and humidity sensor are performed within the climate chamber. The climate chamber is a certified calibration tool, which can generate temperatures between -30 till 50°C and a humidity level (depending on the temperature) between $10 - 90\%$. Within the chamber, various reference sensors are placed. Again, the calibration results in a calibration curve, which describes the temperature/humidity dependent bias. After the bias correction, the temperature sensor has an accuracy of $\pm 0.3^{\circ}$, whereas the Humidity sensor has an accuracy of $\pm 1\%$. Figure 4.2 shows the calibration curves of both temperature and humidity.

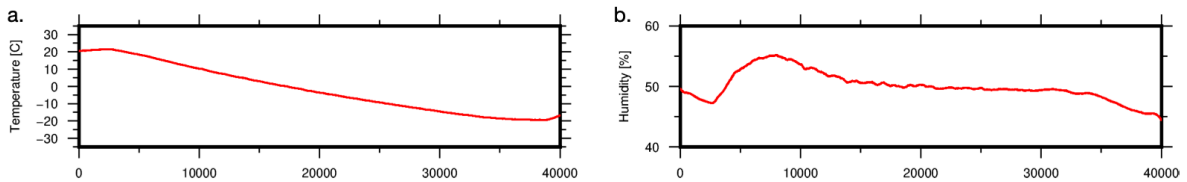


Figure 4.2: Calibration curve of the temperature sensor (panel a) and humidity sensor (panel b).

4.2. Field comparison

The field tests of the monitoring platform have been performed within building K of the KNMI. This building is placed at the border of the KNMI test field. Building K is a shelter and provides an energy supply for the monitoring system. However, for direct and correct comparison between the meteorological MEMS with the KNMI sensor network, it is recommended to perform future comparisons outside building K. The remainder of geophysical parameters are correctly sensed from building K.

4.2.1. Meteorological observations

The LPS sensor has been field-tested along with a Paroscientific Digiquartz 1015A barometer, which has an accuracy of 0.05 hPa. Figure 4.3 shows the comparison between the Multi-EAR (red line) and the barometric reference sensor (black line). It stands out that both sensors resolve the changing barometric pressure. From the distribution of observations, it has been estimated that the LPS sensor has a precision of ± 0.1 hPa for 87% of the time. For the remainder, the maximum deviation was ± 0.2 hPa.

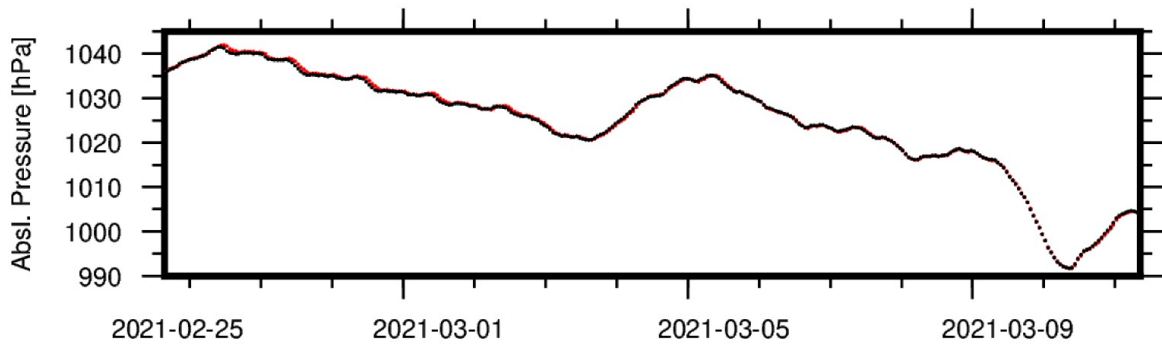


Figure 4.3: Barometric pressure comparison between the Multi-EAR (red line) and the KNMI sensor (black line) at the KNMI test field.

The comparison between the Multi-EAR's temperature has been performed with the reference sensor. The maximum temperature is correctly resolved by the Multi-EAR. The minimum temperatures (occurring during the night), however, are not correctly resolved. This is due to the monitoring circumstances, building K conserves the 'day-warmth'.

The same phenomena occurs with the humidity sensor. The humidity within building K is continuously below the actual meteorological humidity. Therefore a correct comparison between the Multi-EAR's humidity sensor and the KNMI reference sensor can not be performed.

4.2.2. Sound observations

The Multi-EAR enables monitoring of a broad acoustic frequency range. The audible spectrum is measured by the Microphones. Over the audible frequency range the RMS of the Sound Pressure Level (SPL) has been derived in decibels (dB). The KNMI test field does not contain an audible reference sensor. Therefore a direct comparison is not possible. Figure 4.5 shows the RMS dB analysis of the microphone recordings. Note that during the night the SPL levels are lower as during the day. Moreover, a small decrease in SPL has been noted during the weekends, relatively to week-days.

The infrasonic wavefield is monitored by the KNMI mini-MB (den Ouden et al., 2021). Figure 4.6 -a

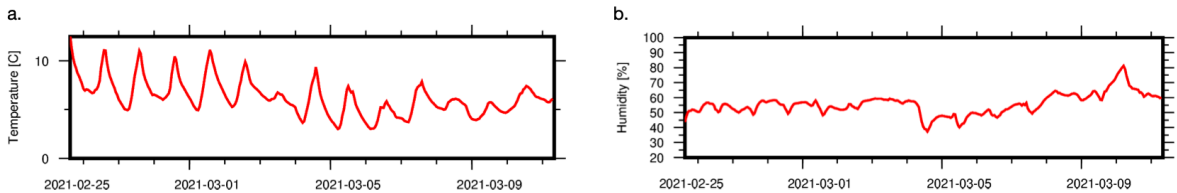


Figure 4.4: Temperature and humidity measurements by the Multi-EAR. The measurements are obtained within building K, therefore a comparison between the Multi-EAR and KNMI sensors is not possible.

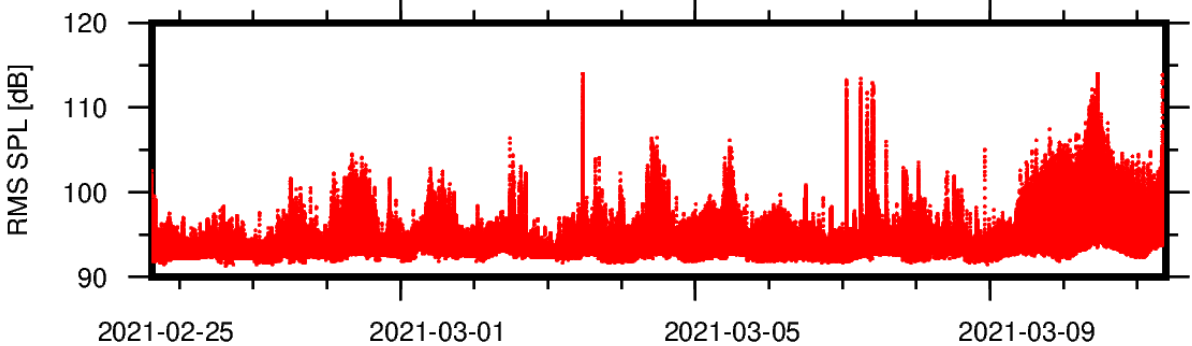


Figure 4.5: Audible sound measurement. Over time the Multi-EAR records the RMS of Sound Pressure Level in decibels over the entire frequency range.

shows the PSD's calculated from the KNMI mini-MB recordings. Panel b shows the PSD's calculated from the infrasonic reference sensor at the KNMI test field, a Hyperion IFS-5000. The gray dotted lines indicate the global high and low noise curves (Brown et al., 2014). Based on a visual comparison between both sensors, it can be noted that the KNMI mini-MB is able to resolve the characteristic microbarom peak around 0.2 Hz. Microbaroms are known to be one of the most omnipresent ambient noise sources within the infrasonic wavefield. Moreover, it can be noted that the KNMI mini-MB is suffering from self-noise within the higher frequencies.

Although the KNMI mini-MB does not resolve the complete ambient noise field, the sensor is able to resolve most of it. Transient infrasonic events (e.g., explosions, earthquakes, volcanic eruptions) have a higher amplitude level compared to the ambient noise. Therefore, any infrasonic explosion will most likely be detected by the KNMI mini-MB.

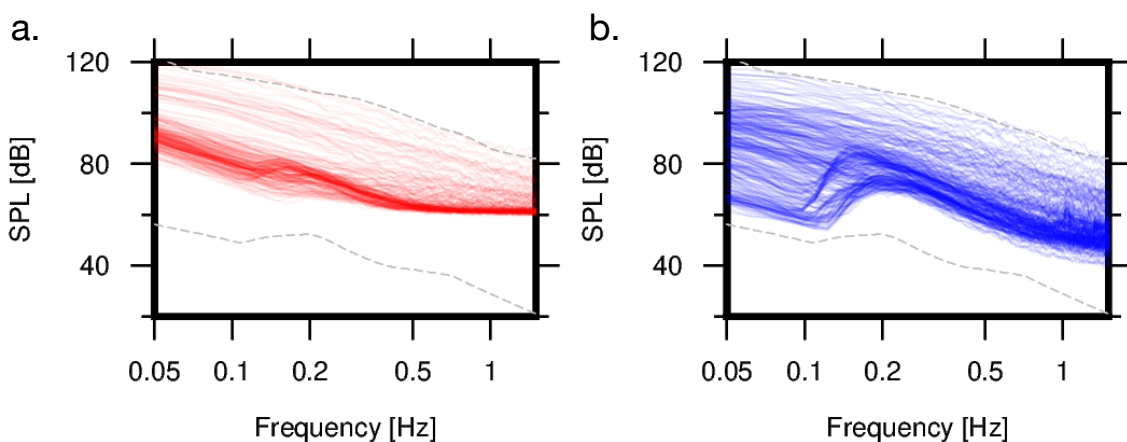


Figure 4.6: Infrasonic wavefield measurement by the KNMI mini-MB (panel a) and a Hyperion xx (panel b). The gray dotted lines indicate the global high and low noise curves (Brown et al., 2014). Note that both sensors resolve the characteristic microbarom peak around 0.2 Hz. Within the higher frequencies the KNMI mini-MB is suffering of sensor self-noise.

4.2.3. Movement observations

Within den Ouden et al., 2021 a comparison test has been carried out in the seismic pavilion of the KNMI. Inside this pavilion, a Streckeisen STS-2 seismometer connected to a Quanterra Q330, is installed as reference sensor KNMI, 1993. All sensors were installed on pillars, to ensure a good coupling between the subsurface and the sensor. The comparison test shows that, although the sensors are deployed on the same seismic pillar and are thus subject to similar seismic noise conditions, the MEMS sensor could not measure ambient seismic noise (McNamara and Buland, 2004; Peterson, 1993) due to its high self-noise level. The MEMS accelerometer exceeds both the U.S. Geological Survey New High Noise Model (NHNM) (Peterson, 1993) and the STS-2 reference sensor by at least 30 dB.

For the comparison between the two accelerometers on the Multi-EAR the z-components of both sensors has been used. The full recordings are divided into hourly recordings, which are used to calculate PSD's. The reference sensor in the seismic pavilion confirms no major seismic activity has been recorded (blue PSD's in Figure 4.7). Therefore, only ambient seismic noise is expected within the recordings.

Figure 4.7 shows the stacked PSD's for the LSM (panel a) and LIS (panel b) MEMS sensors. The solid gray lines indicate the high and low ambient seismic noise curves (McNamara and Buland, 2004; Peterson, 1993). The MEMS don't resolve ambient noise signals, due to their high self-noise. However, note that the self-noise levels of the different MEMS sensors is not similar. The LIS has a lower self-noise compared to the LSM, while the ADC has the same amount of bits (Sleeman et al., 2006). Sometimes ADC's are suffering a 'loss of bits' due to power supply. Whenever the efficiency of the MEMS is lacking, the ADC may suffer from a low-voltage supply, which results in this loss. The LIS sensor includes an accelerometer and gyroscope, whereas the LSM includes an accelerometer and magnetometer. The combination of various sensors within one MEMS may influence the efficiency of power towards the ADC, explaining the difference in self-noise.

Based on Figure 4.7 it can be concluded that the MEMS will not resolve ambient seismic noise signal. However, the MEMS will resolve signals with an amplitude above the self-noise levels. The dotted black lines within both panels of the figure indicate the expected amplitude levels of earthquakes with an approximate distance of 10km (nearby transient sources) [cite raspberry shake manual]. Those theoretical amplitude curves lie above the self-noise levels of both MEMS.

The MEMS of the Multi-EAR are not for monitoring purposes of ambient seismic noise or teleseismic events. Previous studies drew similar conclusions concerning the performance of MEMS accelerometers. Various calibration set-ups are considered while comparing MEMS accelerometers with conventional accelerometers of geophones (Albarbar et al., 2009; Anthony et al., 2019; Hons et al., 2008), each concluding that the accuracy of the MEMS is not sufficient for recording ambient seismic noise. However, strong local events or boisterous environments the MEMS sensor will resolve those seismic signals.

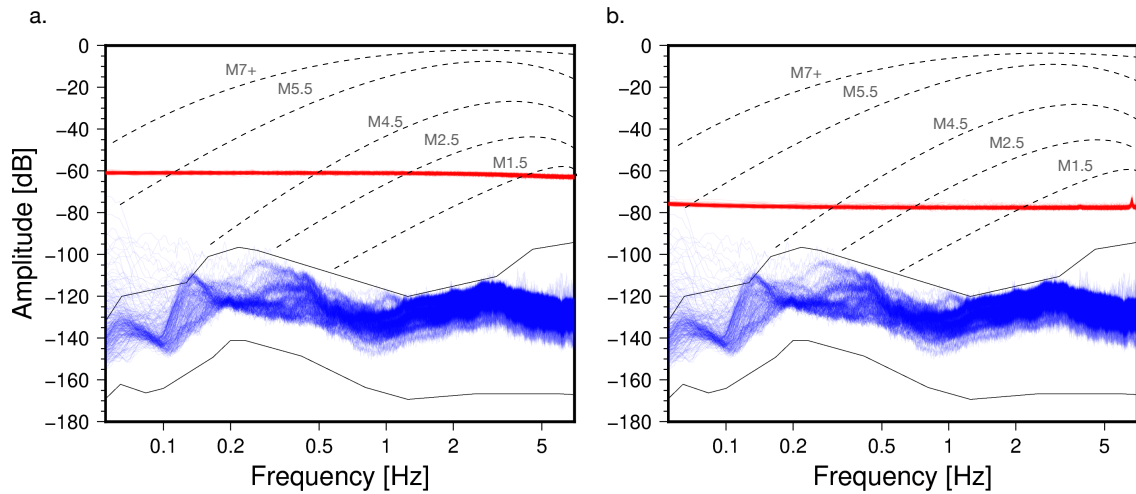


Figure 4.7: Power Spectral Density curves, hourly calculated for the LSM (red lines, panel a), the LIS (red lines, panel b), and the reference sensor (blue lines in both panels). The solid gray lines indicate the global high and low ambient seismic noise curves (McNamara and Buland, 2004; Peterson, 1993). The dotted lines indicate the theoretical amplitude levels of a nearby transient event.

5

Outlook

We propose to integrate the Multi-EAR within the KNMI/TU-Delft sensor network. A low-cost mobile platform will complement the existing network, and allows higher spatial resolution data.

Having a low-cost mobile platform enables:

- High spatial-temporal sampling of multiple geophysical parameters, which can be used for validation of the KNMI's high-resolution weather models.
- Quality measurements on unique locations where the network is sparse (on sea or at land/sea transitions, on volcano's, drones, balloons, the Cabauw tower).
- Allows measurement of meteorological circumstances that can be very local (fog, thunderstorms, sleet) and so improve the code orange/red alarms from province regions to zip code regions.
- Rapid deployments in predicted code orange/red scenarios for which there is interest to collect more field data.
- Environmental deployments at remote places (e.g., local glacier or geothermal monitoring).

Furthermore, such a platform has a high innovative character and scientific quality:

- Research-grade mobile geophysical platform that allows for the selection of specific sensors and sample rates.
- Ability to sample multidisciplinary data on one platform.
- Agility to install sensors at strategic locations to better assess specific events, like aftershocks of an earthquake or severe weather to support.
- Low energy consumption, which facilitates deployment at a wide variety of locations as well as on drones and high-altitude balloons.
- The design of the mobile platform uses the latest trends in miniature sensor technology, and 3D print technology.
- The calibration of the sensor follows high quality standards that have been developed at the KNMI.
- The observations provide information of natural hazards on much higher time- and spatial-scales; allowing for mesh-scale and local scale observations in natural hazards research (convective storms, volcano monitoring)

Collaborative projects

This monitoring platform is ready for integration within field campaigns, or existing monitoring network. E-Surfmar is one of the first collaborative partners. This project is part of EUMETNET (European Meteorological Service Network) and lead by Marijn de Haj (KNMI-RDWD). Within the E-Surfmar a barometer comparison have been performed. Pressure is the most important parameter measured at sea for Numerical Weather Prediction. Meteorological services (NMS) are used to equip voluntary observing ships with high level standard barometers, with a low uncertainty and drift. However, the sources of uncertainties on pressure measurements on a ship are numerous (e.g., changing height of barometer, wind effects, waves, air conditioning).

Barometer prices vary between a few tens until several thousands of euros. Therefore it is worth while to test, and compare, various barometers in a calibration lab, as well as in real conditions. Inter-comparison will show the measurement quality, robustness, and cost/benefit ratio over longer periods of deployment. The study will focus on digital barometers that can easily be integrated in the TurboWin+ software, on which Automatic Pressure Report solutions are already available for some NMS.

Future projects

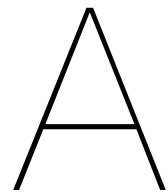
The Multi-EAR is interesting to use as monitoring platform for various studies. One study is focused on the Cabauw Tower, a collaboration within the Ruisdael observatory (KNMI/TU-Delft). The tower consists of various geophysical sensors, including an infrasound array. Therefore the Cabauw facility allows to be a good 'environmental' reference facility.

Besides the ability to use the tower as a reference, the tower experiences turbulence and movement due to weather. It is unknown how these movements influence the measurements at different heights of the tower. Furthermore, it is unknown how the tower is influenced by gravity waves. Therefore, a multidisciplinary sensor platform, which measures acceleration as well as meteorological and infrasonic parameters is favourable. The existing high-fidelity sensor network at the tower will benefit from the added data by the low-cost sensor platform.

Furthermore, the sensor platform can be used on hot-air - and weather/scientific balloon observations in collaboration with the KNMI (De Bruijn et al., 2020). Hot-air balloons provide stable measurement conditions, the balloons experience less turbulence as the static Cabauw tower. Besides hot-air balloons, the sensor platform can be attached to a radiosonde, which is able to fly at a more constant altitude. Those observations give insights in changing of various geophysical parameters with altitude and can be used to determine lightning, severe weather development (outflow), as well as sea breeze fronts. Furthermore, those observations are crucial in understanding the behaviour of the boundary layer and its influence on infrasonic wave propagation.

Moreover, the Multi-EAR can be used as TU-Delft campus array. Currently, the Delft tech-campus is not equipped with a seismo-acoustic array. However, there are plans for a geothermal well on campus. Therefore it is important to perform seismo-acoustic measurements to determine the vibrations, caused by the drill activity. Such measurements are of importance whenever damage occurs.

Finally, the Multi-EAR has the ability to become an educational platform. It can be used as education platform for primary and secondary schools, introducing children with technology and physics. Besides, the platform can be used by university under-grad students during fieldwork courses. Creating a measurement campaign, acquisition of own data, data processing it, and analysing.



Firmware update

The firmware can be updated through the "Hermes" software package. Hermes can be downloaded from the GitHub repository.

- Connect the sensor platform with the TU-Delft laptop via the connector pins (Figure A.1).



Figure A.1: Connect the Pins of the Laptop in the order; Black-Green-White, to the monitoring platform.

- Open Hermes

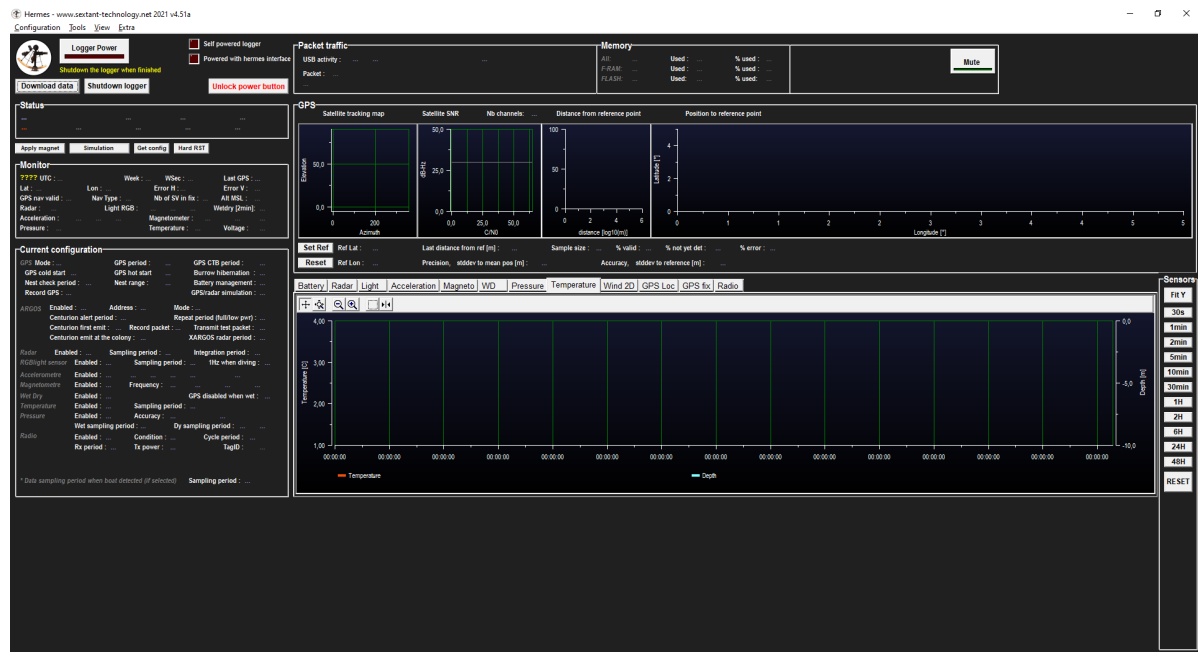


Figure A.2

- Go to; "Tools - Firmware". Import the new firmware. An example can be found on the GitHub.

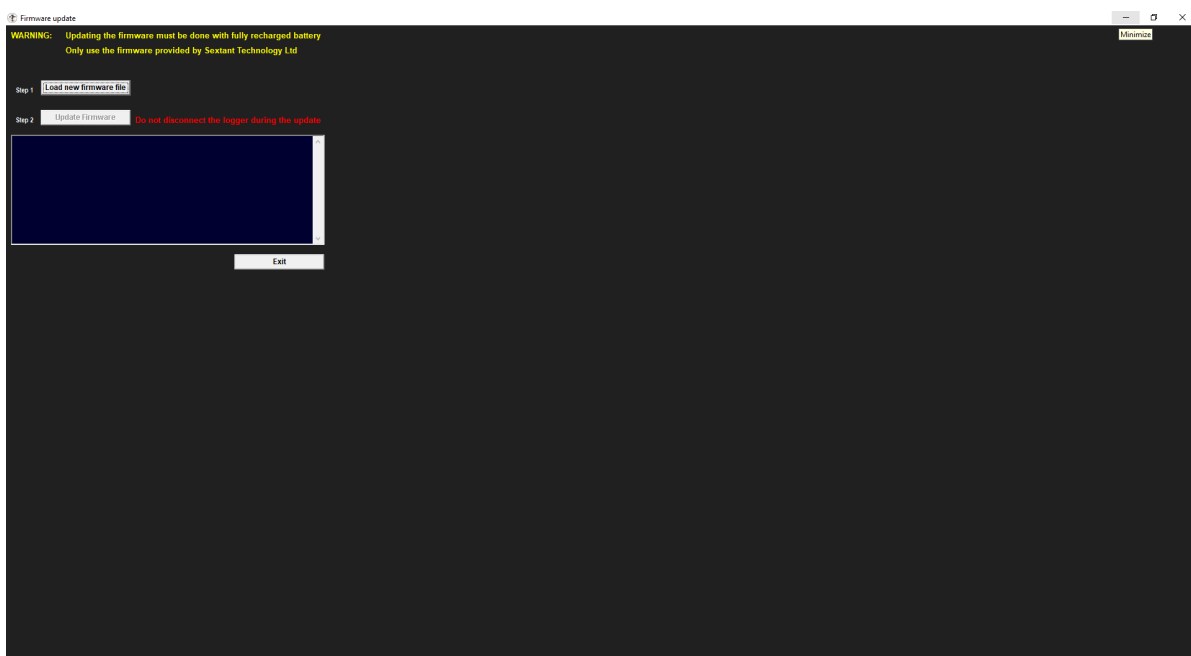


Figure A.3

- To see if and how the data is logged. Go to; "Tools - Logbook" and start Logging. Within the middle window the data will appear and the logging is shown.

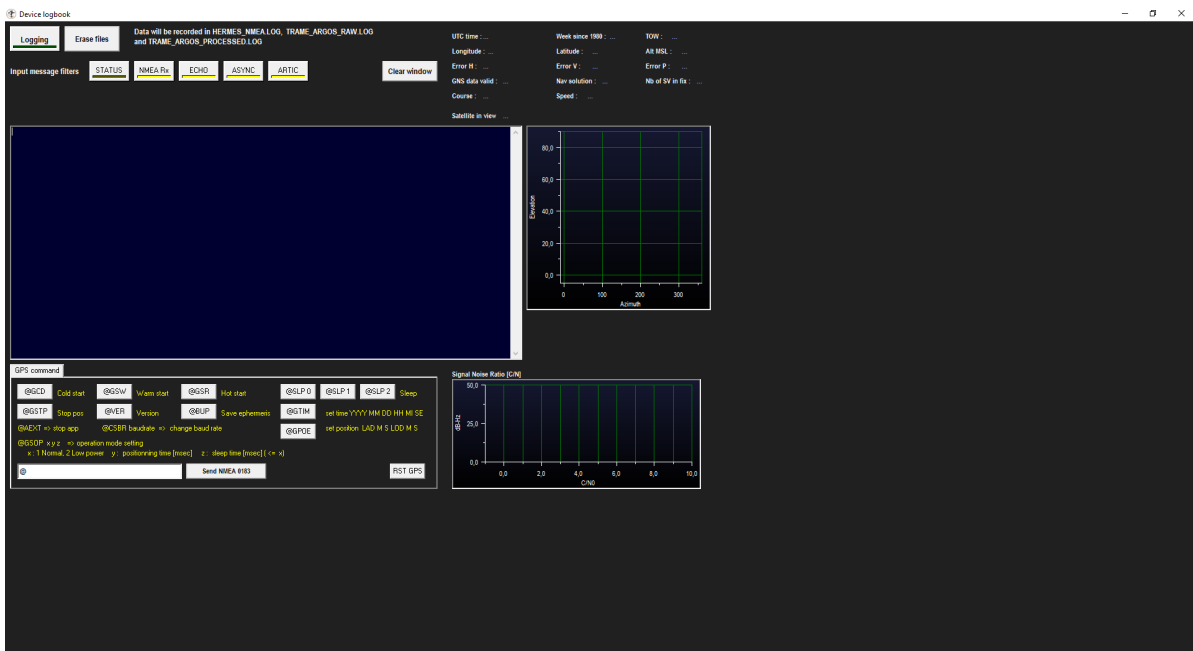


Figure A.4

B

UART serial data communication

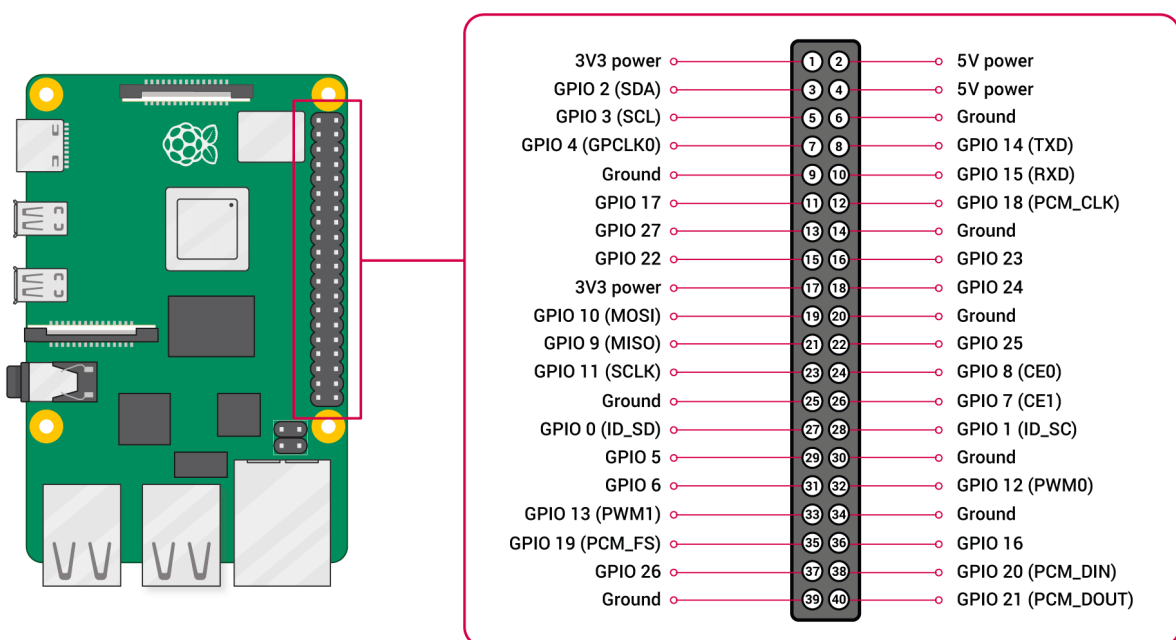
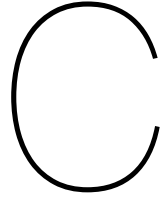


Figure B.1: Overview of the RPi and the GPIO header.

The RPi and the Multi-EAR can be connected via the GPIO header (Figure B.1). The GPIO delivers via the RPi a continuous power supply for the PCB. Besides a power supply, the GPIO header allows a data transfer between PCB and RPi. Therefore, the RPi can act as data logger.

Pins 8 and 10 are the UART serial pins. These pins allow serial data communication between RPi and PCB. Via the TXD (pin 8) the RPi can send commands, while the RXD (pin 10) is used by the PCB to send data.

The RPi receives on a pre-specified baud-rate the data in bytes. The byte string starts with a start-byte, when-after the check-sum comes, before the actual data floats in. The start-byte is used for logging. The data is stored within log-files, each start-byte used to start a new line. The python script for receiving, and logging the data, is available on the GitHub. Afterwards the data can either be formatted to floats, integer, or actual units.



Output sensor platform byte structure

The output of the Multi-EAR, according the firmware, per sample cycle is organised as follows:

Byte	value	description
0	0x11	synchronization byte
1	0x99	synchronization byte
2	0x22	synchronization byte
3	0x88	synchronization byte
4	0x33	synchronization byte
5	cmd	0x73 (= Multi-EAR PACKET COMMAND)
6	packet size	size of the packet without the synchronization bytes
7	CRC16 L	16CRC computed on payload lower byte
8	CRC16 H	16CRC computed on payload upper byte
9	payload[0]	DATA.bits within byte 9
10	payload[1]	DATA.bits within byte 10
11	payload[2]	DATA.bits within byte 11
9+n	payload[n]	DATA.bits within byte n

Table C.1: Byte output Multi-EAR

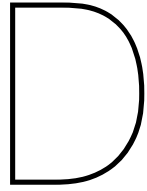
The payload can be subdivided as:

- 0 GPS - 3 bytes
- 1 Infrasound sensor - 2 bytes
- 2 Empty, 2 bytes
- 3 Barometric pressuere - 3 bytes
- 4 LIS3DH Accl - 2 bytes per axis (x,y,z)
- 5 LSM303 Accl - 2 bytes per axis (x,y,z)
- 6 SHT8x Temperature - 2 bytes
- 7 SHT8x Humidity - 2 bytes
- 8 Microphones - 2 bytes

Data Processing Levels

The Multi-EAR's data products can be subdivided into different levels, between 0 and 4. These data processing levels match the [NASA Data Processing Levels](#). Level 0 represents the raw data bytes. Higher data levels indicated the amount of conversion of the raw recording into more useful parameters and formats.

- **Level 0** Unprocessed instrument and payload data at full resolution. Including all communications artifacts (e.g., synchronization frames, communications headers). Format of level 0 data is bytes.
- **Level 1** Unprocessed instrument and payload data at full resolution, time-referenced, and annotated with ancillary information, including calibration coefficients and other metadata. Format of level 1 data is floats.
- **Level 2** Derived geophysical variables at the same resolution and location as Level 1 data. Format of level 2 data is floats.
- **Level 3** Compressed Level 2 data. MSEED files are used to compress the Level 2 data. Format of level 3 data is not the full resolution in floats, but the difference between data samples in floats.



XML metadata

Theoretical response functions

The theoretical response functions of the audible sensors, as described within Chapter 2, are included within the XML files as Poles and Zeros.

The meteorological response functions are included within the conversion equations from bytes/floats into real units. These equations are described within the next section of this appendix.

Conversion to geophysical values

Barometric pressure

The barometric pressure sensor, the LPS33HW, is a digital MEMS and returns 3 data bytes. The H, L, and XL bytes (Level 0 data). Combining these results in a float (Level 1 data). Applying the following scaling to the float enables to express the data into actual geophysical units (Level 2 data):

$$\text{Press [hPa]} = \text{float}/4096 \quad (\text{D.1})$$

Temperature and Humidity

The temperature and humidity sensor, the SHT8x, is also a digital MEMS and returns 2 data bytes. The S_{RH} and S_T bytes (Level 0 data). Applying the following scaling to this data enables to express the bytes into actual geophysical units (Level 2 data):

$$\text{RH}[\%] = 100 * \frac{S_{RH}}{2^{16} - 1} \quad (\text{D.2})$$

$$T[^\circ\text{C}] = -45 + 175 * \frac{S_T}{2^{16} - 1} \quad (\text{D.3})$$

KNMI mini-MB

The DLVR sensor, which is the sensing element of the KNMI mini-MB, returns two bytes (Level 0 data), which are combined into a float (Level 1 data). Using the equation below converts the raw output into actual units:

$$\text{Press [Pa]} = (2.5 * FS * (\frac{P_{out} - O_S}{2^{14}}))/250 \quad (\text{D.4})$$

where FS indicates the full scale of the pressure range. The Multi-EAR's full range is ± 125 Pa.

Microphone

The microphones are the only analogue MEMS on the PCB. An ADC has been connected to the microphones to converted the analog signals into a digital output. The output of the microphone are milli-volts, and can directly be converted into a decibel value with the following equation:

$$\text{Press [dB]} = 20 * \log_{10}(\frac{S}{1000}) \quad (\text{D.5})$$

where 1000 mV/Pa is the reference output ratio.

Accelerometers

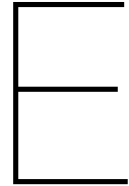
Both accelerometers are 3-axis (x, y, and z-component). Each component is expressed in 2 bytes as raw output (Level 0 data). Combined into floats (Level 1 data), the actual units are obtained by multiplying these with the scaling values of the MEMS.

Whenever the LSM sensor is measuring on the highest-resolution it uses 12 of the 14 bits, due to the "loss-of-bits". Whenever the power consumption of the LSM is too high, the resolution can be decreased into 10 or 8bits. The scaling factor of the LSM for varying ranges and resolution are summarized in the table:

The LIS sensor can only measure at the highest-resolution rate, using 12 of the 14 bits. The scaling factor is:

- **Range 2g :** 1365
- **Range 4g :** 4096
- **Range 8g :** 8190
- **Range 16g:** 16380

LSM303			
Range	12-bit	10-bit	8-bit
2g	0.98	3.90	15.63
4g	1.95	7.82	31.26
8g	3.90	15.63	62.52
16g	11.72	46.9	187.59



SSH connection with RPi

To access the RPi and the sensor platform's data over WiFi, an SSH connection is required. Within this appendix a guideline is provided to create a SSH connection.

First, the RPi needs to be connected with the local WiFi network.

- For an SSH connection it is required to connect the RPi with the local WiFi network. To do; eject the SD-card from the RPi and inject in the TU-Delft laptop.
- Open the SD-cards folder. And navigate towards the file "WPAsupplicant.conf"
- Within this file all possible WiFi connections are stored. Adding the local network is done by inserting:

Listing E.1: WPA example

```
country=NL
ctrl_interface=DIR=/var/run/wpa_supplicant GROUP=netdev
update_config=1

network={
    ssid="WIFI_SSID"
    scan_ssid=1
    psk="WIFI_PASSWORD"
    key_mgmt=WPA-PSK
}
```

- Change the "ssid" into the name of the local WiFi network.
- Change the "psk" into the password of the local WiFi network.
- Whenever the local network is within an institute (e.g., KNMI, TU-Delft, School), the inserted code within the WPA will look like:

Listing E.2: WPA example

```
country=NL
ctrl_interface=DIR=/var/run/wpa_supplicant GROUP=netdev
update_config=1

network={
    ssid="WIFI_SSID"
    key_mgmt=WPA-EAP
    eap=PEAP
    phase2="auth=MSCHAPV2"
    identity="yourUsername@yourInstitution"
    anonymous_identity="anonymous@yourInstitution"
    password="YOUR_WIFI_PASSWORD"
}
```

Second, the IP-adress of the RPi.

- Before a SSH connection can be made between laptop and RPi over the local network, the IP-adress of the RPi on the local network needs to be found.
- The IP-adress is similar to a post-adress. Each device that is connected to the local WiFi network has an unique IP-adress, which can be used to communicate with.
- The IP-adress can be found by using an IP-adress app (e.g., 'fling').
- Whenever such an app is connected to the local network, it will list all the devices on the network, including the RPi - and show the IP-adress.

Third, the SSH connection

- By knowing the IP-adress an SSH connection can be made between the TU-Delft laptop and the monitoring platform.
- Open Putty, and fill in the IP-adress.

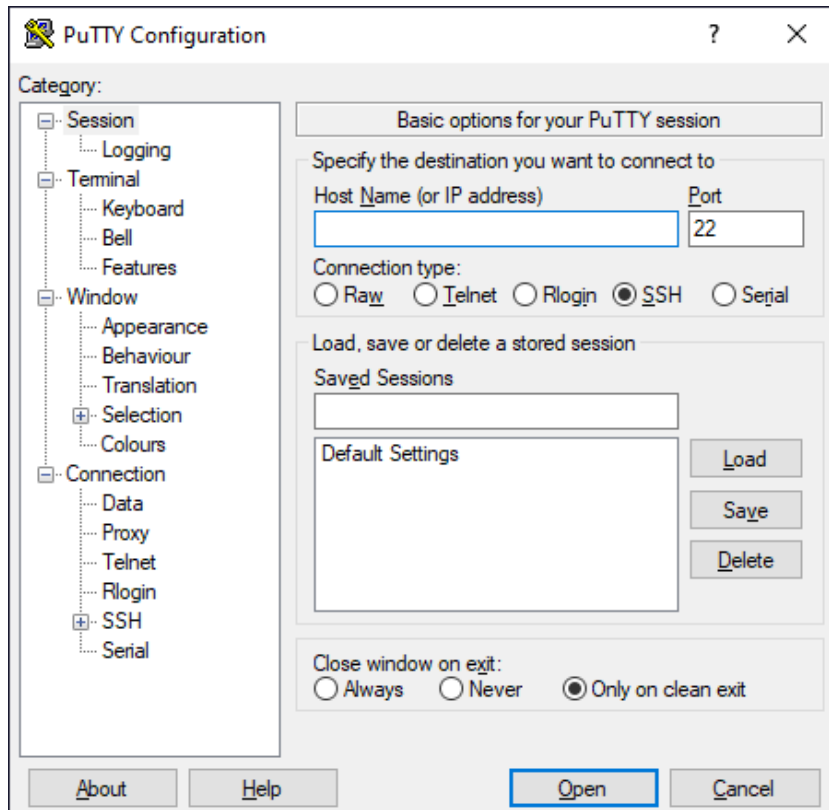


Figure E.1

- Now an SSH connection is made between laptop and Multi-EAR. Log in to the Multi-EAR, within the pop-up window, by entering the Password: raspberry.

Finally, accessing the Multi-EAR data

- Thanks to the SSH connection, it is possible to access the Multi-EAR remotely. The data can be found within the folder '/pi/home/data/'

F

Pictures

F.1. Sensor platform

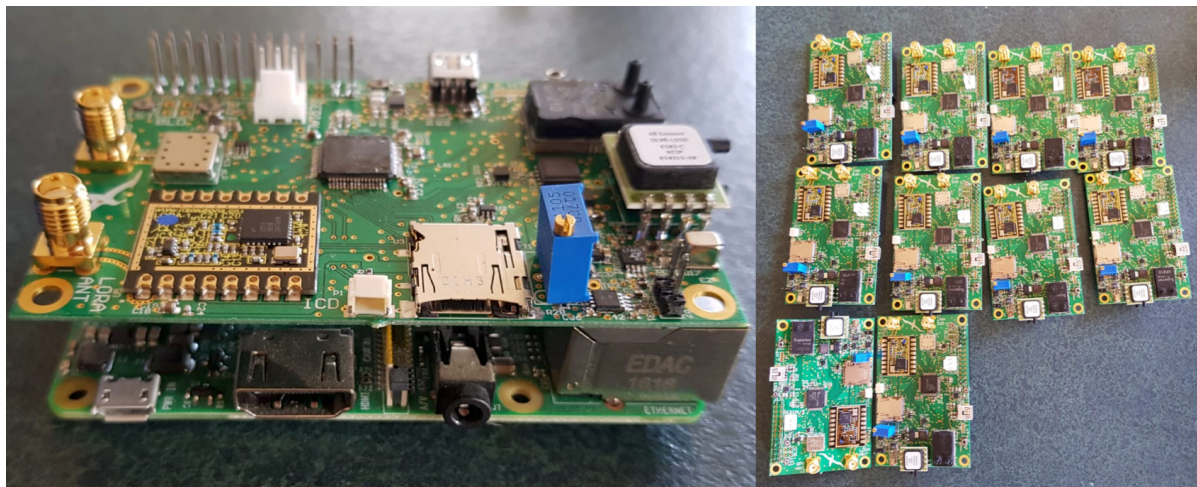


Figure F.1

F.2. Small casing - (serial numbers 3001 - 3022)



Figure F.2

F.3. Large casing - (serial numbers 3101 - 3108)



Figure F.3

F.4. Power supply



Figure F.4

F.5. Antenna's



Figure F.5

G

Low-costs sensor platform

Within this appendix an overview of the total costs for **one** sensor platform are summed.

Sensors	
Barometric pressure	€5,35
Temperature and Humidity	€25,15
Differential pressure sensor	€40,55
Microphone	€2,54
Accelerometer and Magnetometer	€2,24
Accelerometer and Gyroscope	€1,25
GPS	€11,95
LoRa	€28,75
Microcontroller	
Microcontroller	€12,95
PCB	
Resistors	~ €15.00
Connectors	~ €15.00
Headers	~ €2.00
PCB screws	~ €3.00
PCB	~ €70.00
Data logger	
RPi	€37,55
SD-card	€12,75
Casings	
Antenna	€13,30
SMA cable	€9,95
Amphenol connector	€14,95
5V adapter	€6,50
Capillary	€16,00
Enclosure	€10,50
3D print Resin	€4,50
Total	€384.73

Bibliography

- Albarbar, A., Badri, A., Sinha, J. K., & Starr, A. (2009). Performance evaluation of mems accelerometers. *Measurement*, 42(5), 790–795.
- Anderson, J. F., Johnson, J. B., Bowman, D. C., & Ronan, T. J. (2018). The gem infrasound logger and custom-built instrumentation. *Seismological Research Letters*, 89(1), 153–164.
- Anthony, R. E., Ringler, A. T., Wilson, D. C., & Wolin, E. (2019). Do low-cost seismographs perform well enough for your network? an overview of laboratory tests and field observations of the osop raspberry shake 4d. *Seismological Research Letters*, 90(1), 219–228.
- Brown, D., Ceranna, L., Prior, M., Mialle, P., & Le Bras, R. J. (2014). The idc seismic, hydroacoustic and infrasound global low and high noise models. *Pure and Applied Geophysics*, 171(3-5), 361–375.
- Campus, P., & Christie, D. (2010). Worldwide observations of infrasonic waves. *Infrasound monitoring for atmospheric studies* (pp. 185–234). Springer.
- D'Alessandro, A., Luzio, D., & D'Anna, G. (2014). Urban mems based seismic network for post-earthquakes rapid disaster assessment. *Advances in Geosciences*.
- De Bruijn, E. I., Bosveld, F. C., de Haan, S., & Heusinkveld, B. G. (2020). Measuring low-altitude winds with a hot-air balloon and their validation with cabauw tower observations. *Journal of Atmospheric and Oceanic Technology*, 37(2), 263–277.
- den Ouden, O. F. C., Assink, J. D., Oudshoorn, C. D., Filippi, D., & Evers, L. G. (2021). The infra-ear: A low-cost mobile multidisciplinary measurement platform for monitoring geophysical parameters. *Atmospheric Measurement Techniques*, 14(5), 3301–3317. <https://doi.org/10.5194/amt-14-3301-2021>
- EU SCIENCE HUB; PVGIS. (2021).
- Fang, Z., Zhao, Z., Du, L., Zhang, J., Pang, C., & Geng, D. (2010). A new portable micro weather station. *2010 IEEE 5th International Conference on Nano/Micro Engineered and Molecular Systems*, 379–382.
- Haak, H. W., & De Wilde, G. (1996). *Microbarograph systems for the infrasonic detection of nuclear explosions*. Royal Netherlands Meteorological Institute, Seismology Division.
- Homeijer, B., Lazaroff, D., Milligan, D., Alley, R., Wu, J., Szepesi, M., Bicknell, B., Zhang, Z., Walmsley, R., & Hartwell, P. (2011). Hewlett packard's seismic grade mems accelerometer. *2011 IEEE 24th International Conference on Micro Electro Mechanical Systems*, 585–588.
- Hons, M., Stewart, R., Lawton, D., Bertram, M., & Hauer, G. (2008). Field data comparisons of mems accelerometers and analog geophones. *The Leading Edge*, 27(7), 896–903.
- Huang, Q.-A., Qin, M., Zhang, Z., Zhou, M., Gu, L., Zhu, H., Hu, D., Hu, Z., Xu, G., & Liu, Z. (2003). Weather station on a chip. *SENSORS, 2003 IEEE*, 2, 1106–1113.
- KNMI. (1993). Netherlands Seismic and Acoustic Network [10.21944/e970fd34-23b9-3411-b366-e4f72877d2c5].
- Ma, R.-H., Wang, Y.-H., & Lee, C.-Y. (2011). Wireless remote weather monitoring system based on mems technologies. *Sensors*, 11(3), 2715–2727.
- Marcillo, O., Johnson, J. B., & Hart, D. (2012). Implementation, characterization, and evaluation of an inexpensive low-power low-noise infrasound sensor based on a micromachined differential pressure transducer and a mechanical filter. *Journal of Atmospheric and Oceanic Technology*, 29(9), 1275–1284.
- Marty, J. (2019). The ims infrasound network: Current status and technological developments. *Infrasound monitoring for atmospheric studies* (pp. 3–62). Springer.
- McNamara, D. E., & Buland, R. P. (2004). Ambient noise levels in the continental united states. *Bulletin of the seismological society of America*, 94(4), 1517–1527.
- Merchant, B. J. (2015). Hyperion 5113/gp infrasound sensor evaluation. *Sandia Report SAND2015-7075, Sandia National Laboratories*.
- Nief, G., Talmadge, C., Rothman, J., & Gabrielson, T. (2019). New generations of infrasound sensors: Technological developments and calibration. *Infrasound monitoring for atmospheric studies* (pp. 63–89). Springer.

- Peterson, J. R. (1993). *Observations and modeling of seismic background noise* (tech. rep.). US Geological Survey.
- Ponceau, D., & Bosca, L. (2010). Low-noise broadband microbarometers. *Infrasound monitoring for atmospheric studies* (pp. 119–140). Springer.
- Raspel, R., Abbott, J.-P., Webster, J., Yu, J., Talmadge, C., Alberts II, K., Collier, S., & Noble, J. (2019). New systems for wind noise reduction for infrasonic measurements. *Infrasound monitoring for atmospheric studies* (pp. 91–124). Springer.
- Slad, G. W., & Merchant, B. J. (2016). Chaparral model 60 infrasound sensor evaluation. *Technical Report*, SAND2016-1902.
- Sleeman, R., Van Wettum, A., & Trampert, J. (2006). Three-channel correlation analysis: A new technique to measure instrumental noise of digitizers and seismic sensors. *Bulletin of the Seismological Society of America*, 96(1), 258–271.
- Sutherland, L. C., & Bass, H. E. (2004). Atmospheric absorption in the atmosphere up to 160 km. *The Journal of the Acoustical Society of America*, 115(3), 1012–1032.
- Technical Report 9W, 6V, Solar panel. (2020).
- Technical Report Amphenol three pin connector. (2018).
- Technical Report DLVR Series Low Voltage Digital Pressure Sensors. (2019).
- Technical Report ICS-40300 microphone. (2021).
- Technical Report Large Casing. (2021).
- Technical Report Linx antenna. (2021).
- Technical Report LIS3DH MEMS sensor. (2021).
- Technical Report LoRa Telecommunication. (2021).
- Technical Report Raspberry Pi Model 3B+. (2018).
- Technical Report SHT8x temperature/humidity sensor. (2021).
- Technical Report SMA cable. (2021).
- Technical Report Small Casing. (2021).
- Technical Report STMicroelectronics LPS33HW. (n.d.).
- Technical Report STMicroelectronics LSM303. (n.d.).
- Technical Report Texim Europe GNS2301. (n.d.).
- Technical Report V75 Battery Pack. (2020).
- Waxler, R., & Assink, J. (2019). Propagation modeling through realistic atmosphere and benchmarking. *Infrasound monitoring for atmospheric studies* (pp. 509–549). Springer.